Penetration of filamentary structures into the divertor region of spherical tokamaks

D. A. Baver and J. R. Myra

Lodestar Research Corporation, 2400 Central Avenue P-5, Boulder, CO 80301, USA

October 2018

submitted to Phys. Plasmas

DOE-ER/ 54678-13 LRC-18-178

LODESTAR RESEARCH CORPORATION

2400 Central Avenue

Boulder, Colorado 80301

Penetration of filamentary structures into the divertor region of spherical tokamaks

D. A. Baver and J. R. Myra

Lodestar Research Corporation, Boulder, CO 80301, USA

Abstract:

Understanding the penetration from the midplane region towards the divertor plate of filamentary structures in the main scrape-off layer of spherical tokamaks is of interest for divertor design and plasma material interaction. Insight into this problem is gained by studying the closely related problem of the parallel structure of resistive ballooning modes, localized to a particular flux surface by a perturbed blob-like density profile. The resulting linearized equations are solved using the Arbitrary Topology Equation Reader (ArbiTER) code. A metric applied to the spatial structure of the dominant eigenmode quantifies mode penetration. Trends in this quantity are then measured by performing parameter scans over temperature and density. The results of this study are consistent with the dominant role of collisionality in limiting mode interaction with the divertor plate.

Keywords: blob, filament, scrape-off layer, tokamak

I Introduction

Coherent filamentary structures, also known as "blobs," or "blob-filaments" are of great importance in determining the transport properties of the scrape-off layer of tokamaks and spherical tokamaks. Coherent structures in edge turbulence were first observed many years ago with probes.[1] Their dominant outward motion in the scrape-off layer [SOL] and the implications for SOL convective transport were subsequently elucidated.[2] Additional historical, theoretical and experimental background is given in several review articles.[3,4]

For the purposes of this discussion a blob-filament may be defined as a flux tube of plasma that consists of higher density and pressure than the surrounding region. Blob-filaments typically extend for many meters along the magnetic field line and have dimensions of the order of a few cm across the magnetic field.

Blob-filaments represent strong order unity density fluctuations in the SOL and their radial convection contributes a large fraction, estimated to be of order 50% of the particle flux in the far SOL.[5,6] They are therefore important for understanding plasma-material interactions on the main chamber walls and other machine hardware. On the other hand, the radial motion of blobs near the separatrix in the near SOL may help to broaden it, providing beneficial spreading of the heat exhaust channel.

The parallel extent of filamentary structures along the field lines is obviously critical for assessing the impact of parallel plasma fluxes on the divertor plates. However, the parallel electrical connection to the plates also determines the flow of plasma current internal to the filament, and therefore plays an important role in determining the regime and velocity of perpendicular propagation.[1-6]

Several theoretical works have investigated questions related to the parallel structure. Easy compared the properties of seeded blob filaments in simple 2D models with 3D fluid simulations.[7] Angus also employed 3D fluid simulations to understand 3D effects and the role of the parallel electron response and drift wave dynamics.[8] Ryutov carried out a theoretical study of isolated plasma filaments in the ideal magnetohydodynamic limit.[9] Walken explored filament dynamics in the MAST experiment using SOL flux tube geometry.[10] Magnetic shear effects were studied theoretically by Stepanenko.[11] Blobs dynamics in 3D for circular flux surface geometry were also included in the turbulence simulations of Halpern.[12]

On the experimental side, measurements of blob filaments by Maqueda *et al* show a lack of time delay between fluctuations at the outboard midplane and the divertor target,[13] implying that these structures extend in the field-parallel direction between the two. On the other hand, they also observed a change in character between structures close to the outer strike point and those further out. Observations by Scotti *et al* likewise observed a correlation peak at zero time delay, implying a field-aligned structure that does not propagate in the parallel direction.[14] However, they also observed a reduction in fluctuations and upstream correlation near the separatrix. A similar reduction in

fluctuations near the separatrix was observed by Walkden *et al*, who reported a quiescent region near the x-point.[15]

These observations suggest that blob-filaments are able to connect between the outboard midplane and the divertor plates, but that this connection is not consistent or universal. The question of interest therefore is to determine the degree of connectivity in these filaments and the conditions on which that connectivity depends. Analytical work[16] and reduced-dimensionality turbulence simulations[17] have pointed out the roles of magnetic geometry and collisionality, but in rather simplified models which could only account for x-point effects in a rather heuristic fashion. The basic idea is that magnetic geometry and collisionality are synergistic: collisionality or more specifically parallel resistivity impedes parallel current flow requiring currents to close across the magnetic field; magnetic geometry near an x-point creates thin flux-tube "fans" across which perpendicular current can more easily flow, essentially through a geometric enhancement of the ion polarization current.

Mechanisms other than collisionality which can limit the parallel extent of modes near an x-point are also possible, notably the finite ion gyro-radius effect proposed by Ryutov and Cohen.[18] In this model the parallel structure of the mode is shorted out near an x-point by cross-field currents which are carried collisionally by the electrons; the ions are unresponsive to the mode because the thin magnetic flux fans increase the effective $k_\perp$ of the mode, and hence result in $k_\perp \rho_i \gg 1$ and orbit averaging. Simulation of this effect would require the use of a kinetic or gyro-kinetic code which can treat the x-point and SOL region in divertor geometry. This is beyond the scope of the present work.

The present work seeks to answer the parallel structure and mode penetration question using linear stability calculations in realistic spherical tokamak geometry in a collisional fluid model. Our motivation in this paper is not to make calculations for any particular experiment, but rather to explore the characteristics of filamentary structures in typical spherical tokamak geometries. The qualitative conclusions of our study are not restricted to spherical tokamaks, and should apply to tokamaks in general; however, our motivation is to develop capabilities for future comparisons with measurements in NSTX-U and MAST-U. Previous work[16] has found a correspondence between nonlinear filamentary structures and the corresponding linear dispersion relation. This correspondence allows a linear calculation, such as employed here, to shed insight into the spatial structures of these blob-filaments. The question of primary importance in this paper is the relationship between blob penetration towards the divertor plate and basic plasma parameters such as temperature and density.

The paper is organized as follows. Section II describes the computational tools employed in these calculations. Section III describes the model equations and coordinate systems employed by these tools. Section IV describes the numerical results and their implications. Section V presents a summary and conclusions.

II ArbiTER

The computational analysis in this article is performed using a code called the Arbitrary Topology Equation Reader, or ArbiTER.[19]

The ArbiTER code is a system for discretizing and solving linear partial differential equations. In this system, the equation sets, profile functions, topological information and definitions of differential operators are loaded from a series of input files. Then, beginning with topology and differential operators, the code uses a series of matrix operations to build up a matrix equation corresponding to that equation set. This matrix equation may be a generalized eigenvalue problem:

$$Ax = B\lambda x \qquad [1]$$

or a source-driven problem:

$$Ax = b \qquad [2]$$

In either case, the resulting matrix equation is passed to a standard linear algebra package to be solved. In the case of source-driven problems, ArbiTER uses the PETSc[20] package. For eigenvalue problems, which are the more common use of this code, it uses the SLEPc[21] package.

The flexibility of the ArbiTER code is useful for many types of problems. Its ability to handle complex topology allows it to treat advanced magnetic geometries in field-line-following coordinates. Also, its flexibility in model equations allows terms to be added or removed, allows a given set of equations to be modeled in multiple topologies, or allows a given topology to be used in multiple equation sets or even types of equations (i.e. solving an eigenvalue and a source-driven problem on the same domain). For the present purposes, however, the ArbiTER code is used primarily as a more advanced version of its predecessor, the 2DX code.[22]

In addition to the ArbiTER code, a number of Python and Mathematica scripts are used for data processing and visualization.

III Procedure

A. Coordinate system

This study is performed using model equations defined in field-line following coordinates. These are also used by BOUT[23] and by most of the turbulence models built under the BOUT++[24] framework. Field-line following coordinates as implemented here are discussed in greater detail in Sec. 3 of Ref. 22. This coordinate system is defined by:

$$x = \psi - \psi_s \qquad [3]$$

$$y = \theta \qquad [4]$$

$$z = \zeta - \int_{\theta_0} d\theta\, \nu(\psi, \theta) \qquad [5]$$

where ζ is the toroidal angle, θ is a poloidal angle variable, ψ is the poloidal flux, and ν is the local safety factor. Because of toroidal symmetry of the equilibrium, the dependence of instabilities on the z coordinate can be represented through a superposition of Fourier modes, that is to say, for an arbitrary

perturbed quantity *Q*, we express $Q = Q_0(x,y)e^{inz}$, where n is the toroidal mode number. This leaves a 2D coordinate space in which to represent and numerically solve model equations. The use of field-line following coordinates and the extraction of the e^{inz} term removes the most rapid variation for moderate and high n eigenmodes analytically.

This coordinate system results in a number of geometric profile functions. These will not be discussed in detail here, but one, the binormal (approximately poloidal) wavenumber k_b, is of importance in defining the equations in the next section:

$$k_b = -nB/RB_p \quad [6]$$

$$RB_p = |\nabla\psi| \quad [7]$$

where R is the major radius, $B_p$is the poloidal magnetic field, and ψ is the poloidal flux coordinate.

B. Equation model

As mentioned in the Introduction, filamentary structures, sometimes called blob-filaments or simply blobs, are field aligned regions of enhanced density and pressure and are universally observed in the SOL of toroidal devices. They are generally believed to be formed by turbulence near or inside the separatrix and can propagate into the SOL by the mechanism of curvature and ∇B charge polarization.[2-4] While a study of the formation and radial propagation of these structures requires a non-linear turbulence model, much can be learned about the *parallel* structure of these filaments from linear theory. This is because the non-linear dynamics enters primarily through the polarization and $E \times B$ nonlinearities which directly affect only the *perpendicular* structure and motion. Thus, the linear stability of closely related modes can provide insight into physical properties of these filamentary structures, such as their parallel connection length. The use of linear theory, explored here, brings with it all the usual advantages including computational efficiency and accuracy, convenience for parametric scans, and direct control of inputs such as toroidal mode number.

The equations used here to model filamentary structures by this technique are based on a resistive ballooning model, which is in turn a subset of a 6-field Braginskii model [19]. The equations of the resistive ballooning model in the Bohm normalization (i.e. with time scaled to the inverse ion gyro-frequency, space to a reference ion gyro-radius, and potential to T_e/e) are as follows:

$$\gamma\nabla_\perp^2\delta\phi = \frac{2B}{n_e}C_r\delta p - \frac{B^2}{n_e}\partial_\parallel\nabla_\perp^2\delta A \quad [8]$$

$$\gamma\delta n_e = -\delta v_E \cdot \nabla n_e \quad [9]$$

$$-\gamma\nabla_\perp^2\delta A = \nu_e\nabla_\perp^2\delta A - \mu n_e\nabla_\parallel\delta\phi \quad [10]$$

where

$$\delta p = (T_i + T_e)\delta n_e \quad [11]$$

$$C_r \equiv \vec{b} \times \kappa \cdot \nabla \quad [12]$$

$$\delta v_E \cdot \nabla \mathrm{Q} \equiv -\mathrm{i}\frac{k_b(\partial_r Q)}{B}\delta\phi \quad [13]$$

The parallel derivative operators are $\nabla_\parallel = \vec{b} \cdot \nabla$ and $\partial_\parallel Q = B\nabla_\parallel(Q/B)$, where Q is a generic equilibrium profile, and $\nabla_\perp^2$ is the perpendicular (to **B**) Laplacian. Eq. 8 uses the Boussinesq approximation on its left-hand side. Eq. 10 includes finite electron mass, but the overall model is still electrostatic. Temperature is not evolved by this equation set; evolution of temperature can be achieved by including more terms and equations from the original Braginskii model, but this would add little to the goals of this paper.

The sheath boundary conditions for this model are given by:

$$\delta J = \frac{n_e\sqrt{T_e+T_i}}{T_e}\delta\phi \quad [14]$$

where $\delta J = \nabla_\perp^2 \delta A$. In the preceding equations, γ is the growth rate, $\delta\phi$, δA and δn_e are the perturbed electrostatic potential, normalized vector potential and density respectively, $B = |\boldsymbol{B}|$ is the background magnetic field, C_r is the curvature operator, δp is the perturbed pressure, δv_E is the perturbed $E \times B$ drift, ν_e is the normalized electron Coulomb collision frequency and $\mu = m_i/m_e$.

C. Magnetic geometry and profile functions

The magnetic geometries used in this article are based on EFIT reconstructions from the NSTX and MAST experiments. However, the experimentally measured plasma temperature and density profiles are replaced by profiles of our own choosing for purposes of parametric scans. As such, these equilibria do not reflect results achieved by any actual experiment, and moreover are not guaranteed to be in equilibrium from a magnetic pressure balance point of view. Instead, these magnetic geometries are taken as "typical" spherical tokamak geometries, and are subject to the approximation that plasma beta in the scrape-off layer is low enough that the magnetic equilibria are not significantly deformed by modifying the pressure profiles. Our motivation in this paper is not to make predictive or interpretative calculations for any particular experiment, but rather to explore the characteristics of filamentary structures in generic or typical spherical tokamaks.

These EFIT reconstructions are run through a series of scripts to convert this data from R-Z coordinates to field line following coordinates. These scripts also calculate geometric profile functions such as curvature, binormal wavenumber, and so forth. A sample plot of the calculated flux surfaces is shown in Fig. 1.

The temperature and density profiles employed here in the radial direction are based on tanh-like functions. In addition, the density profile has a Gaussian "bump" added to it in the scrape-off layer. The main purpose of this bump is to provide a strong local gradient which localizes a class of eigenmodes to the vicinity of the bump. Related to this is the fact that ArbiTER, being based on a sparse eigensolver, loses its computational advantages over a full-matrix eigensolver if all eigenmodes are

calculated; as such, it only returns a selected number of fastest-growing modes. In order to ensure that the modes localized to a particular flux surface have growth rates sufficient to make it onto that list, the gradient must be increased near the flux surface of interest. While this introduces distortion into the eigenvalues themselves, relative to the tanh-like case, such a compromise is necessary in order to control the radial location of these eigenmodes. In addition to this practical consideration, there is a more physics-based rationale: a filamentary structure (blob) can be approximated as a superposition of resistive ballooning modes of finite toroidal mode number and a perturbation in the background density that is toroidally uniform. Moreover, the correspondence principle for blob motion[3] directly relates the nonlinear blob velocity and structure size to the wavenumber and frequency of the underlying linear modes. The so-called called "blob-dispersion relation" obtained from linear theory has been shown to agree remarkably well with 2D nonlinear simulations (see Fig. 2 in Ref. 16). Thus the bump and the instabilities it produces are directly related to structure of a blob.

These considerations result in profile functions as shown in Fig. 2. In addition, the corresponding temperature profile is shown in Fig. 3. With the exception of the results in section IV.C, these profiles are assumed to be poloidally uniform.

IV Results

A. Preliminary processing

In the section that follows, each ArbiTER simulation returns the 30 fastest growing eigenmodes. Despite the use of bump-perturbed density functions, the fastest growing mode is not necessarily the mode of interest. Instead, a script is used to analyze the calculated eigenmodes and to return the fastest growing mode with a peak in its fluctuating quantities that is near (within some specified number of grid cells) of a flux surface of interest.

In addition, this script also calculates a number of parameters of interest, in particular the ratio of mode amplitudes at certain key locations: the outboard midplane on the flux surface of interest, the point nearest the x-point on the flux surface of interest, and the outboard divertor plate on the flux surface of interest.

The simulations in the following section use a resolution of 32 radial points by 64 poloidal points. Doubling the radial resolution for the centermost case in Fig. 9 resulted in a 1.22% increase in the eigenvalue of interest, suggesting that for the sort of conclusions drawn in this paper the modes are adequately resolved.

B. Parameter scans

1. Mode number scan

The first parameter scan to be performed was to calculate growth rates as a function of toroidal mode number. This calculation is important mainly because it helps determine the mode number range of interest for future calculations.

Fig. 4 shows results from this calculation. In both cases, the slope of the curve is significantly lower at n=100 than at lower mode numbers. In theory, this can be explained by the fact that the mode becomes radially narrower at high toroidal mode numbers. This means that at low mode numbers, the mode covers a range of radial positions with different radial gradients, possibly including reversed gradient (good curvature) regions. At higher mode numbers, only the most unstable regions are sampled, so narrowing the mode further has little effect on growth rates. Since the motivation for the bump-on-tail density profile is to emulate the physics of a filamentary structure, the radial scale of the eigenmode should ideally be comparable to the scale of the bump, which should occur near the turning point (i.e. near the upper part of the "knee") in the mode number scan.

Based on this, it appears reasonable to use n=100 as the toroidal mode number in further studies. Since it is known[25] that the growth rate eigenvalues of the ballooning equation for parallel mode structure in the asymptotic limit of large n is independent of n, the parallel penetration results are not expected to be unduly sensitive to this choice. In practice, depending on T_i, finite-Larmor radius effects may significantly impact the growth rates at high n. causing γ(n) to maximize and then decay as n is further increased. Although this effect is not included in the reduced model of the present study, it should be considered for future quantitative experimental comparisons.

2. Density-temperature scans

In order to measure the effects of temperature and density on mode penetration, these parameters were varied. This was accomplished by taking a standard case and multiplying the temperature and density by values ranging from 3 to 1/3, a range which will be seen to encompass the important physical regime transitions.

The mode penetration to the divertor was quantified as follows: first, a field (potential, density, vector potential) was chosen to represent overall mode amplitude; in this case, potential was used. Next, the mode amplitudes at the point along the flux surface of interest nearest the x-point were compared to the mode amplitudes at the outboard divertor leg on the flux surface of interest. While this ratio alone could be used to quantify mode penetration, the trends in this are clearer if one instead uses this ratio to construct a metric defined here as

$$\lambda/L = 1/ln\left(\phi_{xpt}/\phi_{div}\right) \qquad [15]$$

For example, if the mode attenuation in the divertor region were exponential $\phi = \phi_0 e^{-s/\lambda}$ then the relative amplitudes at the x-point and divertor would scale as $\phi_{div} = \phi_{xpt} e^{-L/\lambda}$ where L is the distance along the field line from the x-point to the divertor. Thus we can interpret the λ/L metric as a ratio of an effective parallel mode penetration length to the field line length.

The results of these scans are shown in Figs. 5-6. The points labeled A, B, and C are specific sets of parameters for which the eigenmodes of interest are also shown in the R-Z plane in Figs. 7 and 8.

Superimposed on Figs. 5 and 6 are lines corresponding to $T \propto n^{2/3}$ and $T \propto n^2$. These reflect the expected behavior of these modes in the disconnected ($\lambda/L < 1$) and sheath-connected ($\lambda/L \sim 1$)

regimes, respectively. In the disconnected regime, mode penetration is expected to be determined by collisionality. Since collisionality varies with $n/T^{3/2}$, the lines of constant collisionality correspond to $T \propto n^{2/3}$. In the sheath-connected regime, on the other hand, mode penetration is influenced by sheath resistivity. Since sheath conductivity varies with $n/T^{1/2}$ (the perturbed sheath current is proportional to the ion saturation current nec_s multiplied by $e\phi/T$), this means that lines of constant sheath resistivity correspond to $T \propto n^2$. This is consistent with the results shown.

C. Results with parallel temperature variation

The calculations in the previous sections assume that temperature is uniform along any given field line. In practice, temperature can vary along field lines especially in the collisional cases. This variation in temperature can potentially alter the mode structure and growth rates of resistive ballooning modes. In order to produce quantitatively accurate estimates of mode structure, it is necessary to take this variation into account.

A simple estimate of parallel temperature variation can be made based on the two-point model.[26] In this model, thermal conductivity is assumed to be limited by collisions, resulting in a temperature that varies according to the following equation:

$$T = \alpha x^{\frac{2}{7}} \qquad [16]$$

where x is the field line length to the divertor plate, plus some finite offset to account for finite plasma temperature at the divertor plate, and α is a constant which depends on power flux and other parameters.

A more accurate model would be to solve a 2D heat conduction equation. However, a nonlinear model of that sort is beyond the scope of this paper, and would be more appropriate for detailed modeling studies than for the present generic explorations.

Instead, the method employed here is to use the two-point model in the divertor leg, and then assume no parallel variation outside the divertor leg. Thus, the parallel temperature variation function is flat between the points facing the x-point, and has the characteristic $x^{2/7}$ dependence in the divertor leg itself. This model can be further simplified by, rather than accounting for the thermal conductivity of the sheath when calculating the offset in Eq. 16, to instead create a floor in the parallel variation function where any value of the function less than the floor is raised to the floor. Once this function has been calculated, it can then be multiplied by any given radial temperature function, giving a resulting temperature profile that equals the radial profile between the points facing the x-point, but falls off with an $x^{2/7}$ dependence in the divertor leg. The density profile is then modified by dividing by this parallel variation function instead of multiplying by it; this keeps pressure constant in the parallel direction.

To assess the effect of parallel variation on the penetration distance, Eq. (15), we computed λ/L using the procedure described in the previous paragraph and compared the result with that obtained using the same radial variation but no parallel variation in the density and temperature profiles.

The results of this comparison are shown in Figs. 9-10. These figures show that the normalized penetration distances in the two cases differ by a nearly constant factor of around 1.8 regardless of temperature or density; while the ratio of penetration distances is not strictly constant, the variation is small given the inherent uncertainties in this type of study.

V Conclusions

The penetration of blob-filaments towards the divertor plate has been modeled using linear analysis of resistive ballooning modes via the ArbiTER code as a proxy for nonlinear analysis of filaments. This has yielded useful insight into the general trends in penetration length with respect to temperature and density.

An analysis of growth rates as a function of toroidal mode number displays a rapid increase followed by a gentle rise, approaching a plateau. This behavior gives an indication of the characteristic toroidal mode number associated with blob-filaments, and thus allows calculations at a single mode number to be used when performing parameter scans over temperature and density.

Analysis of eigenmode structure allows mode penetration to the divertor leg to be quantified in terms of the logarithm of the ratio of mode amplitudes at the x-point and divertor. This calculation produces an effective decay length (corresponding to an exponential decay of the filaments in the parallel direction between the x-point and the divertor plate) that can be compared to experiment and analytical theory.

Making these calculations over a range of values of temperature and density shows quantitative agreement with analytical theory in two limiting cases. In the non-connected case, mode structure is dominated by parallel resistivity, resulting in mode structure that depends on $nT^{-3/2}$. In the connected case, mode structure is dominated by sheath resistivity resulting in mode structure that depends on $nT^{-1/2}$. In addition, accounting for the effects of parallel temperature variation in the divertor leg does not qualitatively change these results.

Although not explicitly demonstrated in this paper, in addition to the resistivity, the location of the bump and the modes it drives also affects the degree of mode connection to the divertor target. Modes localized closer to separatrix tend to be more disconnected in qualitative agreement with experiments:[14,15] λ/L decreases due to increased magnetic shear and magnetic field line length L as the separatrix is approached

In conclusion, our paper illustrates a simple and intuitive heuristic for estimating the penetration of blob-filaments to the divertor plate, and thus for predicting their effect on transport and wall lifetime in the divertor region. Moreover, a quantitative estimate of the transition point between these regimes is also provided.

Acknowledgements

The authors have benefited a great deal from the contributions of their collaborators. In particular, we wish to thank the following people for their contributions: F. Militello, N. Walkden, F. Scotti and S. J. Zweben.

This material is based upon work supported by the U.S. Department of Energy Office of Science, Office of Fusion Energy Sciences under Award Number DE-FG02-02ER54678 ; however, such support does not constitute an endorsement by the DOE of the views expressed herein.

Figures

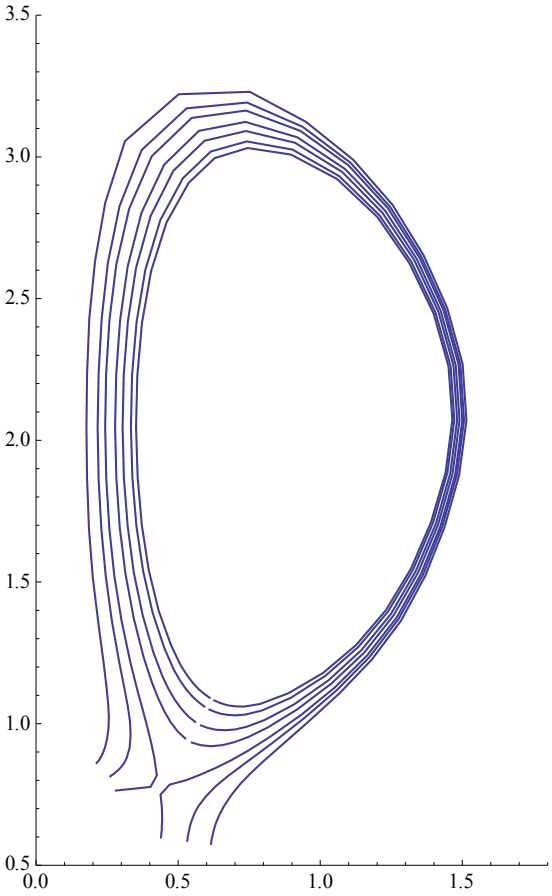

Figure 1: Sample flux surfaces for a typical NSTX-like magnetic geometry. [Associated dataset available at http://doi.org/10.5281/zenodo.2530371] (Ref. 27).

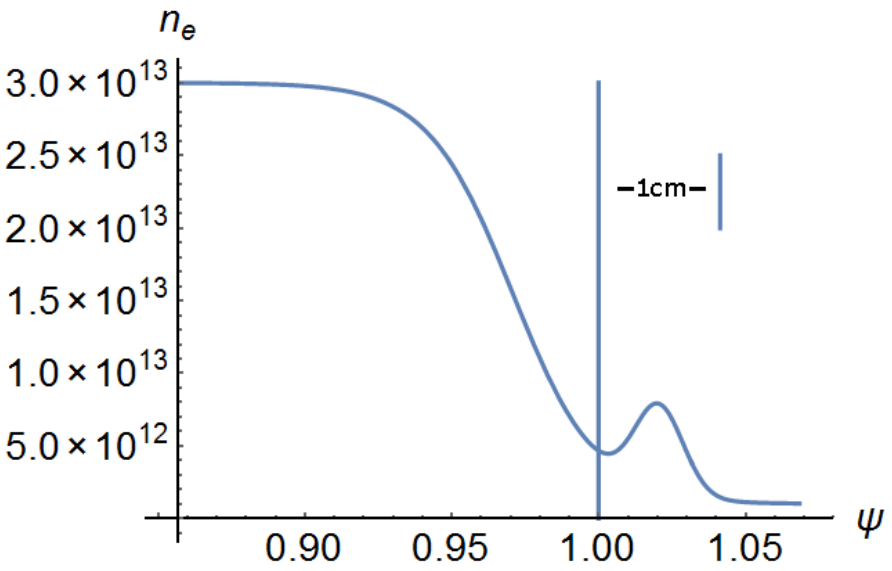

Figure 2: Density as a function of radial flux coordinate (labeled as a fraction of the poloidal flux at the magnetic separatrix) for filament simulations in MAST-like geometry. The density is taken to be a flux function in Sec. IV.B and varies along the field line in Sec IV.C (see text for details). [Associated dataset available at http://doi.org/10.5281/zenodo.2530371] (Ref. 27).

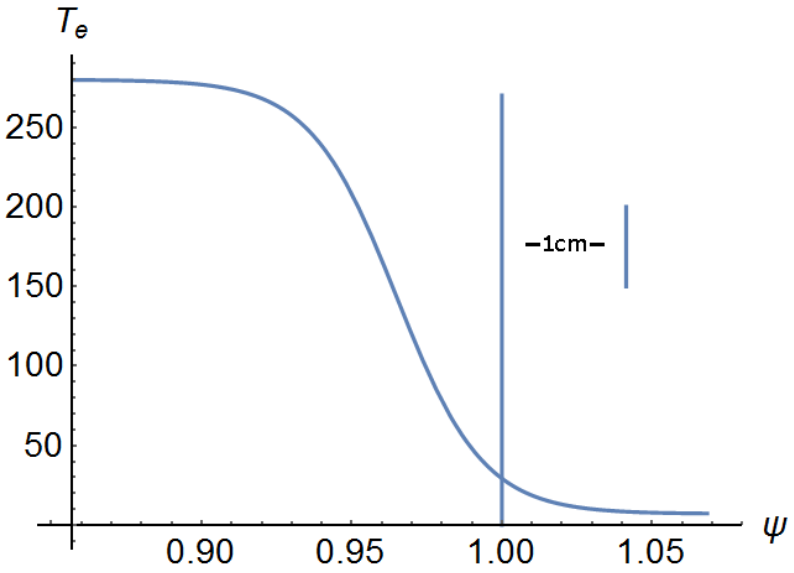

Figure 3: Temperature as a function of radial flux coordinate (labeled as a fraction of the poloidal flux at the magnetic separatrix) for filament simulations in MAST-like geometry. The temperature is taken to be a flux function in Sec. IV.B and varies along the field line in Sec IV.C (see text for details). [Associated dataset available at http://doi.org/10.5281/zenodo.2530371] (Ref. 27).

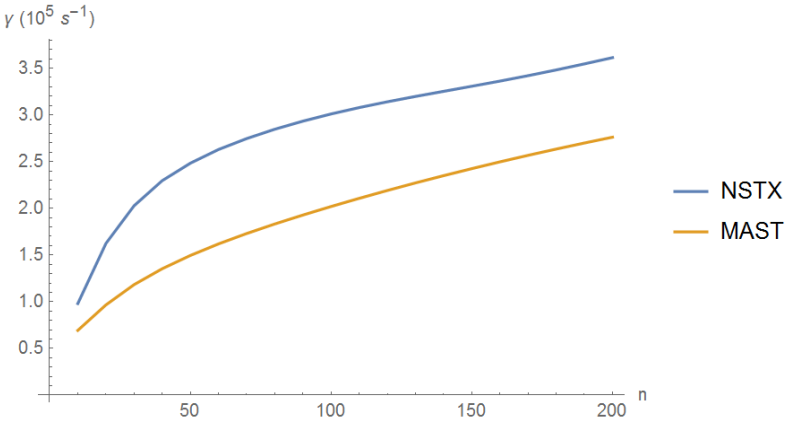

Figure 4: Growth rate as a function of toroidal mode number (n) for NSTX and MAST-like geometries. The NSTX-like case has a density of n_e = 7.9 x 10^{12} cm^{-3} while the MAST-like case has a density of n_e = 5.31 x 10^{12} cm^{-3} at the bump peak. [Associated dataset available at http://doi.org/10.5281/zenodo.2530371] (Ref. 27).

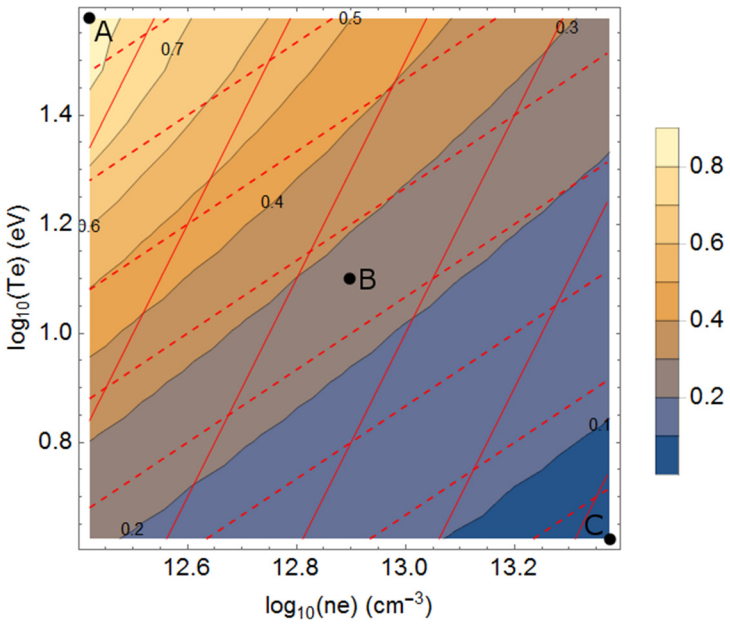

Figure 5: Color-filled contour plot of penetration ratio λ/L as a function of temperature and density at mode peak for toroidal mode number 100 (NSTX-like geometry). Eigenmodes for the parameters

corresponding to the labeled points A, B, and C are shown in Fig. 7. Overlaid solid lines have $T \propto n^2$ and dashed lines have $T \propto n^{2/3}$ and correspond to sheath connected and resistively disconnected asymptotic limits respectively. [Associated dataset available at http://doi.org/10.5281/zenodo.2530371] (Ref. 27).

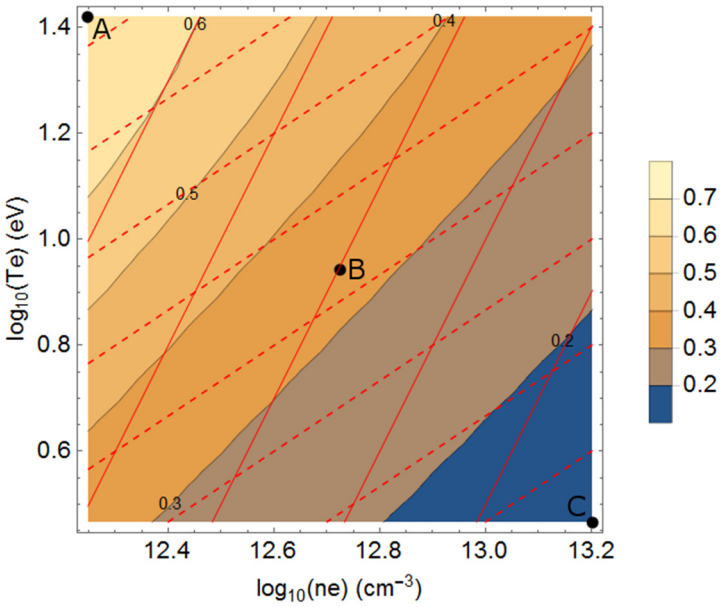

Figure 6: Color-filled contour plot of penetration ratio λ/L as a function of temperature and density at mode peak for toroidal mode number 100 (MAST-like geometry). See Fig. 5 for additional information and Fig. 8 for eigenmode structure. [Associated dataset available at http://doi.org/10.5281/zenodo.2530371] (Ref. 27).

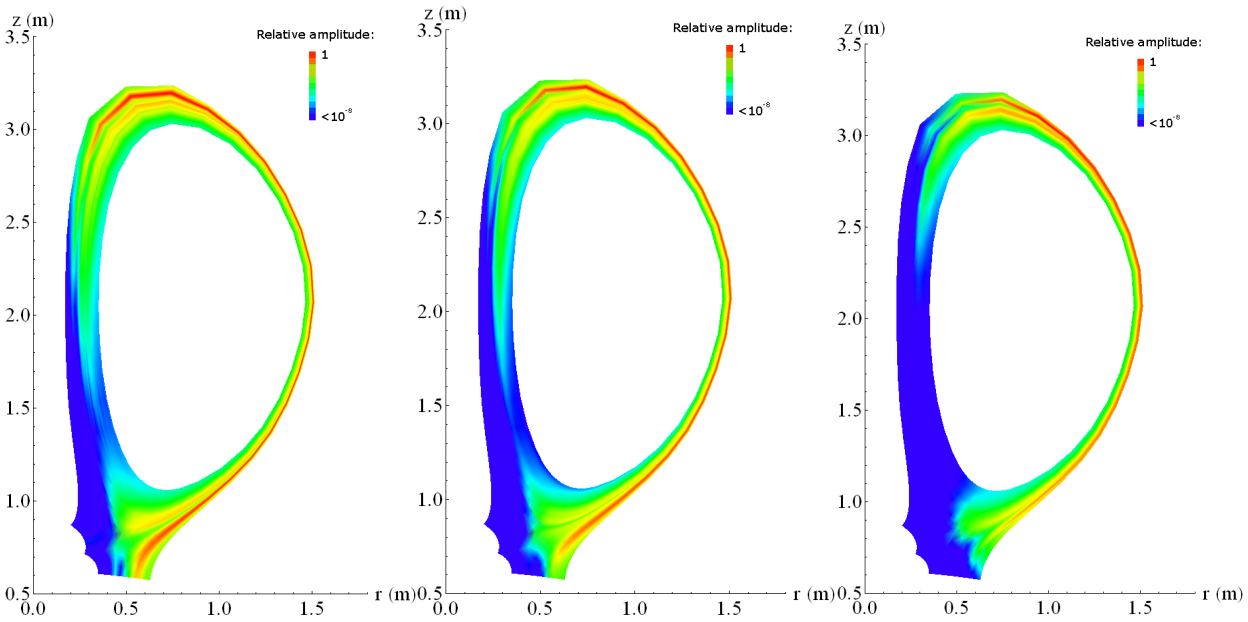

Figure 7: R-Z plot of eigenmode structure for selected NSTX-like-geometry cases (left to right): Bump n_e=2.63x10^{12}, T_e=37.8 eV; Bump n_e=7.9x10^{12}, T_e=12.6 eV; Bump n_e=2.37x10^{13}, T_e=4.2 eV. [Associated dataset available at http://doi.org/10.5281/zenodo.2530371] (Ref. 27).

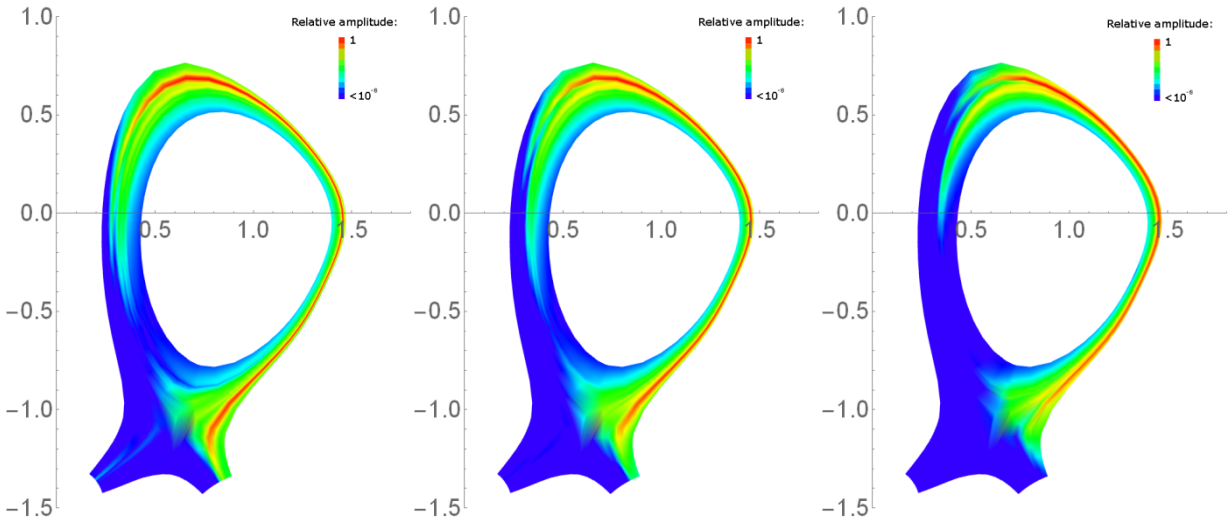

Figure 8: R-Z plots of eigenmode structure for selected MAST-like-geometry cases (left to right): Bump n_e=1.77x10^{12}, T_e=2.92 eV; Bump n_e=5.31x10^{12}, T_e=8.77 eV; Bump n_e=1.59x10^{13}, T_e=26.3 eV. [Associated dataset available at http://doi.org/10.5281/zenodo.2530371] (Ref. 27).

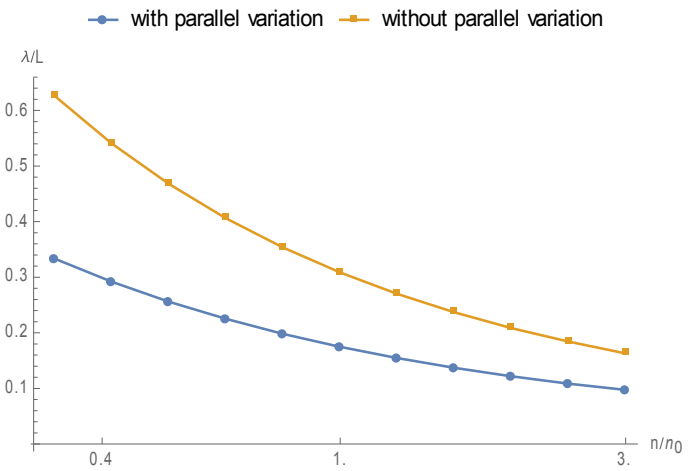

Figure 9: Penetration length as a function of relative density for case without parallel temperature variation (green) and with parallel temperature variation (blue). [Associated dataset available at http://doi.org/10.5281/zenodo.2530371] (Ref. 27).

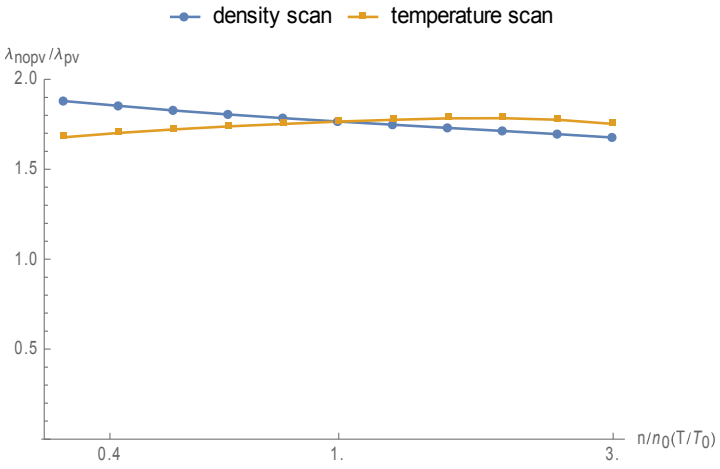

Figure 10: Ratio of penetration lengths of cases without parallel temperature variation over cases with parallel temperature variation, as a function of relative density and relative temperature. [Associated dataset available at http://doi.org/10.5281/zenodo.2530371] (Ref. 27).

References

[1] S. J. Zweben, Phys. Fluids **28**, 974 (1985).
[2] S. I. Krasheninnikov, Phys. Lett. A **283**, 368 (2001).
[3] S. I. Krasheninnikov, D. A. D'Ippolito, and J. R. Myra, J. Plasma Physics **74**, 679 (2008).
[4] D.A. D'Ippolito, J.R. Myra and S.J. Zweben, Phys. Plasmas **18**, 060501 (2011).
[5] J. A. Boedo, D. Rudakov, R. Moyer, S . Krasheninnikov, D . Whyte, G. McKee, G. Tynan, M. Schaffer, P. Stangeby, P. West, S. Allen, T. Evans, R. Fonck, E. Hollmann, A. Leonard, A. Mahdavi, G. Porter, M. Tillack and G. Antar, Phys. Plasmas **8**, 4826 (2001).
[6] D. L. Rudakov, J. A. Boedo, R. A. Moyer, S. Krasheninnikov, A. W. Leonard, M. A. Mahdavi, G. R. McKee, G. D. Porter, P. C. Stangeby, J. G. Watkins, W. P. West, D. G. Whyte and G. Antar, Plasma Phys. Control. Fusion **44**, 717 (2002).
[7] L. Easy, F. Militello, J. Omotani, B. Dudson, E. Havlíčková, P. Tamain, V. Naulin, and A. H. Nielsen, Phys. Plasmas **21**, 122515 (2014).
[8] J. R. Angus, M. V. Umansky, and S. I. Krasheninnikov, Phys. Rev. Lett. **108**, 215002 (2012).
[9] D. D. Ryutov, Phys. Plasmas **13**, 122307 (2006).
[10] N. R. Walkden, B. D. Dudson and G. Fishpool, Plasma Phys. Control. Fusion **55**, 105005 (2013).
[11] A. A. Stepanenko, W. Lee, and S. I. Krasheninnikov, Phys. Plasmas **24**, 012301 (2017).
[12] F.D. Halpern, P. Ricci, S. Jolliet, J. Loizu and A. Mosetto, Nucl. Fusion **54**, 043003 (2014).
[13] R.J. Maqueda, D.P. Stotler and the NSTX Team, Nucl. Fusion **50**, 075002 (2010).
[14] F. Scotti, S. Zweben, V. Soukhanovskii, D. Baver, and J. Myra, Nucl. Fusion **58**, 126028 (2018).
[15] N.R. Walkden, J. Harrison, S.A. Silburn, T. Farley, S.S. Henderson, A. Kirk, F. Militello, A. Thornton and The MAST Team, Nucl. Fusion **57**, 126028 (2017).
[16] J. R. Myra, D.A. Russell and D. A. D'Ippolito, Phys. Plasmas **13**, 112502 (2006).
[17] D. A. Russell, J. R. Myra and D. A. D'Ippolito, Phys. Plasmas **14**, 102307 (2007).
[18] D. D. Ryutov and R. H. Cohen, Contrib. Plasma Phys. **44**, 168 (2004).
[19] D. A. Baver, J. R. Myra and M. V. Umansky, Commun. Comp. Phys. **20**, 136 (2016).
[20] http://www.mcs.anl.gov/petsc
[21] http://www.grycap.upv.es/slepc
[22] D. A. Baver, J. R. Myra, M. V. Umansky, Comp. Phys. Comm. **182**, 1610 (2011).
[23] M. V. Umansky, X. Q. Xu, B. Dudson, L. L. LoDestro, J. R. Myra, Computer Phys. Comm. **180**, 887 (2009).
[24] B. D. Dudson, M. V. Umansky, X. Q. Xu, P. B. Snyder, H. R. Wilson, Computer Physics Communications **180**, 1467 (2009).
[25] J.W. Connor, R.J. Hastie and J.B. Taylor, Proc. Roy. Soc. London, Ser. A **365**, 1 (1979).
[26] P. C. Stangeby, *The Plasma Boundary of Magnetic Fusion Devices* (Institute of Physics Publishing, Bristol, Philadelphia, PA, 2000).
[27] Derek A Baver and James R Myra, "Penetration of filamentary structures into the divertor region of spherical tokamaks," Zenodo.
http://doi.org/10.5281/zenodo.2530371.